

# Large deformation simulation of anisotropic material using an updated Lagrangian finite element method

R.H.W. ten Thije <sup>\*</sup>, R. Akkerman, J. Huétink

*Department of Mechanical Engineering, University of Twente, P.O. Box 217, 7500 AE Enschede, The Netherlands*

Received 4 August 2006; received in revised form 20 February 2007; accepted 21 February 2007

## Abstract

Large deformation finite element (FE) simulations of anisotropic material often show slow convergence or break down with increasing anisotropy and deformation. Large deformations are generally approximated by multiple small linearised steps. This leads to poor performance and contradicting formulations. Here, a new conceptually simple scheme was implemented in an updated Lagrange formulation. An appropriate decomposition of the deformation gradient results in constitutive relations defined in invariant tensors. Consistent tangent matrices are given for a linearly elastic fibre model and for a generalised anisotropic material. The simulations are robust, showing quadratic convergence for arbitrary degrees of anisotropy and arbitrary deformations with strain increments over 100%. Plasticity of the fibres is included without compromising the rate of convergence.

© 2007 Elsevier B.V. All rights reserved.

**Keywords:** Finite element; Anisotropy; Large deformation; Composite; Forming process

## 1. Introduction

Numerical optimization of products and production processes becomes increasingly important in the design phase of composite structures. It can reduce the time to market and can avoid the production of costly prototypes. Numerical simulations of the composite forming processes such as e.g. draping, rubber pressing or diaphragm forming are an essential part of these optimization tools if doubly curved products are considered. Redistribution of the fibres is then inevitable. The resulting fibre orientation is one of the most important parameters to control. These numerical simulations can also reveal problem areas where wrinkling or fibre buckling might occur.

There are two main approaches in composite forming simulations: the geometrical approach and the finite element (FE) approach. The fast and simple geometrical models are often sufficient for design purposes and date back to

the fifties of the past century, where Mack and Taylor predicted the fibre distribution of a woven cloth on simple geometries based on a pin jointed net assumption [16]. Increasingly sophisticated models have been built ever since [23,2,8] and recently even interactive tools that allow the user to virtually manipulate woven fabrics have been developed [9].

FE simulations are capable of simulating the production process in great detail, including mechanisms such as tool-part friction, inter-ply friction, wrinkling and fibre bridging. One of the earliest elastic models was applied by Chen and Govindaraj in the mid 1990s of the past century [6]. These FE simulations are however time consuming and often not very robust. Large deformation FE simulations of highly anisotropic material often show slow convergence or break down with increasing anisotropy and deformation.

The scale of anisotropy in metals is of a different order of magnitude compared to fibre reinforced composites, but recent developments point to the same imperfections in standard FE formulations in this field as well. Inclusion of yielding and plastic flow of anisotropic metals according

<sup>\*</sup> Corresponding author. Tel.: +31 (0) 53 489 2426; fax: +31 (0) 53 489 4784.

E-mail address: [r.h.w.tenthije@utwente.nl](mailto:r.h.w.tenthije@utwente.nl) (R.H.W. ten Thije).

to the Hill, Vegter or Barlat criteria [10,29,3] is a standard option in FE packages nowadays. Extension to large deformations and strains is however not straightforward. Bonet and Burton illustrated that the standard FE formulations are only valid for small or moderate strains [5]. Standard theories are based on the additive decomposition of the linear strain tensor, an assumption that can lead to significant deviations if the simulation is split into multiple steps. Inclusion of anisotropy is only straightforward if the additive structure is preserved according to Sansour and Bocko [26]. A formulation along this line can be found in the work of Lu and Papadopoulos [15], who proposed a covariant formulation of anisotropic plasticity to circumvent problems associated with intermediate configurations that typically result from the small strain theory. It is worth noting at this point that the shortcomings of the small strain theory are independent of the fact that the material is anisotropic, but anisotropy makes the need for accurate descriptions at high strains more eminent or even inevitable.

Nedjar [19–21] and Huétink [13] proposed the use of multiplicative splits of the deformation tensors, which do not necessarily have to be equal for each material fraction. Huétink illustrated the straightforward implementation of fibrous materials in FE simulations by splitting the deformation tensor into a rotation part and a stretch part for each fibre fraction. Anisotropic materials can be efficiently and accurately modelled by implementing several material fractions into one element as shown by Hsiao and Kikuchi [11]. It results in a continuum material formulation with one or more axes of anisotropy. Huétink's approach allows for accurate tracking of multiple fibre directions in one continuum, whereas the use of a classic Green Naghdi or Jaumann approach would lead to poor results because the fibre direction is not exactly followed. These conclusions are stated by Boisse as well [4].

Accurate modelling of the fibre rotations with respect to the reference coordinate system is included in the viscous models of McEntee and ÓBrádaigh and Spencer [17,28]. A different approach was adopted by Yu et al. [31], Peng and Cao [22] and Xue et al. [30] by using non-orthogonal constitutive models. A convected non-orthogonal coordinate system, whose in-plane axes coincides with the two fibre directions, is embedded in elements. The exactness of these models is often compromised on an implementation level where increments are linearised. FE formulations using a hybrid formulation automatically track the fibre direction. Bar or truss elements are coupled to displacement degrees of freedom of continuum elements and their orientation is therefore known exactly. This approach has been used by several researchers [25,27] and was implemented as a standard option in the commercial FE programs ABAQUS<sup>®</sup> and MSC MARC<sup>®</sup>.

### 1.1. Uniaxial tensile test

The following examples illustrate the difficulties when using a standard FE formulation to simulate deformations

of highly anisotropic materials. An arbitrary commercial FE code, ANSYS<sup>®</sup>, is used to simulate a simple tensile test with a ply of unidirectional fibres. The linear elastic material is highly anisotropic with a stiffness ratio of  $1-10^5$ . A mesh of  $15 \times 30$  plane stress quadrilateral elements (PLANE42) is used. The left and right hand side are clamped and the right hand side moves in the  $y$ -direction as shown in Fig. 1. The incremental displacement  $\delta$  is very small, only  $5 \times 10^{-5}$  times the length of the specimen. Geometric nonlinearities are taken into account (NLGEOM, ON). Nevertheless, the simulation breaks down after only four steps at an elongation of only 0.02%. Fig. 1 shows the last converged solution. The ply widens near the clamped edges, while it should contract due to Poisson's effect. Similar results are obtained with other FE codes. This phenomenon is caused by updating the material orientations using an incorrect geometry. The element strains  $\varepsilon$  are found by

$$\{\varepsilon\} = [\mathbf{B}] \cdot \{\mathbf{u}\}, \quad (1)$$

where  $[\mathbf{B}]$  contains the derivatives of the element shape functions and  $\{\mathbf{u}\}$  denotes the nodal displacements. Implicit codes obtain the highest order of accuracy if  $[\mathbf{B}]$  is evaluated on the intermediate geometry between the initial state and the current deformed state. The resulting stresses and subsequently the nodal forces become misaligned if the material orientation is updated using the same intermediate geometry, as illustrated in Fig. 2b. The top node of a single element is moved to the right. As the fibre is the only stress bearing material in the element, the resulting nodal force at the end of the step should be aligned with the new fibre direction. The orientation update should take place using the current geometry to avoid misalignment of the nodal forces in large deformation simulations with anisotropic material (Fig. 2c).

### 1.2. Pure shear

Incorrect deformed shapes can be avoided by evaluating the material tensor using the final geometry. Unfortunately this leads to less accurate strain predictions as shown in the next example. One element is sheared up to  $75^\circ$  as shown in Fig. 3. Applying pure shear should not introduce strains in the fibres which are aligned with the frame. The fibre strain

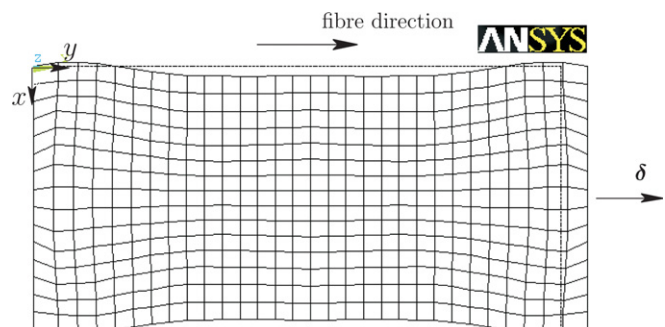


Fig. 1. Deformed shape ( $\times 250$ ) of a tensile test simulation with a highly anisotropic material.

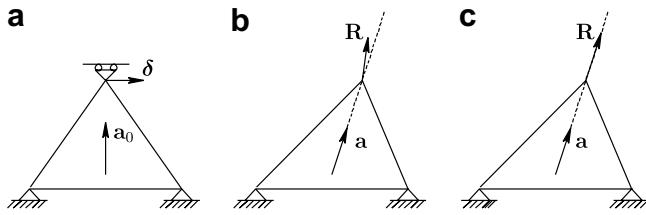


Fig. 2. Resulting (mis-) alignment of the nodal force. (a) initial geometry (b) nodal force  $R$  when using the intermediate geometry (c) nodal force  $R$  when using the final geometry.

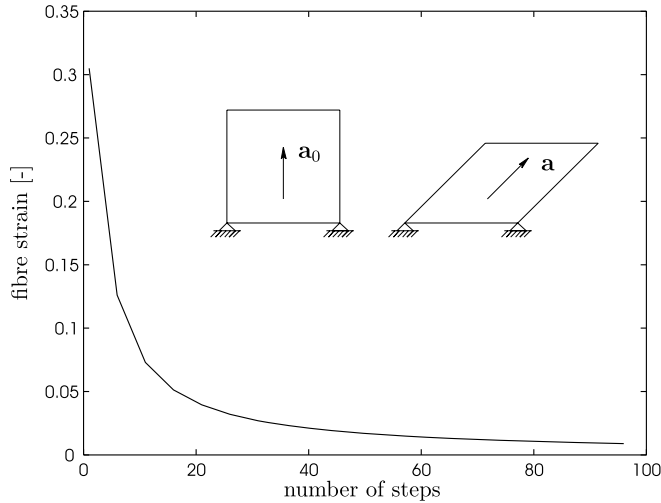


Fig. 3. Inaccurate fibre strain in pure shear.

is however as high as 30% if it is evaluated according to (1) and the deformation is applied in one step. Fig. 3 shows that the accuracy improves if the total deformation is split into several steps, but this increases the calculation time significantly. As much as 86 steps are necessary to reduce the fibre strain below 1%.

The ‘standard’ large deformation simulations are based on the assumption that a large nonlinear displacement can be accurately approximated by multiple small steps in which a linear theory is applied. This assumption leads to poor performance in implicit FE simulations with (highly) anisotropic material. The previous examples illustrate that it leads to contradicting requirements as well. A review of the finite element formulation is necessary if large deformations of anisotropic material are considered.

## 2. Continuum mechanics

Continuum mechanics provides a mathematical description of motion and deformation of material in a reference system. It considers a body of a homogenous material which can be anisotropic.

### 2.1. Kinematics

The deformable body in Fig. 4 is located in space by the Lagrangian vector  $\mathbf{X}$  at time  $t$ . The body has a volume  $V$

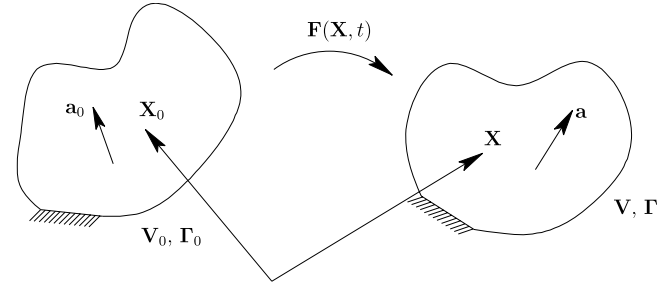


Fig. 4. Initial and current configuration of a body.

and a surface boundary  $\Gamma$ . The location of the material particles in time is defined by the Eulerian location vector  $x$ , which is a function of  $\mathbf{X}$  and  $t$

$$x = x(\mathbf{X}, t). \quad (2)$$

The deformation gradient  $\mathbf{F}(\mathbf{X}, t)$  maps the initial configuration onto the current configuration,

$$\mathbf{F}(\mathbf{X}, t) = \frac{\partial x}{\partial \mathbf{X}} \bigg|_t = x \bar{\nabla}_0 \quad (3)$$

and can be decomposed into a stretch tensor and a subsequent rotation or vice versa. The split is commonly performed using a polar decomposition and results in a symmetrical stretch tensor. An alternative decomposition is more convenient when considering anisotropic materials. The symmetry condition of the stretch tensor is abandoned. The deformation tensor is decomposed in a stretch tensor  $\mathbf{G}$  and a subsequent rotation  $\mathbf{R}$ .

$$\mathbf{F} = \mathbf{R} \cdot \mathbf{G}. \quad (4)$$

We are free to choose any orthonormal rotation tensor  $\mathbf{R}$  such that the non-symmetrical stretch tensor  $\mathbf{G}$  is invariant under rigid body rotations. With the decomposition of (4), the velocity gradient  $\mathbf{L}$  is written as

$$\mathbf{L} = \mathbf{v} \bar{\nabla} = \dot{\mathbf{F}} \cdot \mathbf{F}^{-1} = \dot{\mathbf{R}} \cdot \mathbf{R}^T + \mathbf{R} \cdot \dot{\mathbf{G}} \cdot \mathbf{G}^{-1} \cdot \mathbf{R}^T, \quad (5)$$

where  $\mathbf{v}$  is the velocity. Introducing the tensors  $\mathbf{\Omega}$  and  $\mathbf{L}^G$  as

$$\mathbf{\Omega} = \dot{\mathbf{R}} \cdot \mathbf{R}^T, \quad (6)$$

$$\mathbf{L}^G = \dot{\mathbf{G}} \cdot \mathbf{G}^{-1}, \quad (7)$$

the velocity gradient is split into the skew symmetric spin tensor  $\mathbf{\Omega}$  and an invariant non-symmetric rate of deformation tensor:

$$\mathbf{L} = \mathbf{\Omega} + \mathbf{R} \cdot \mathbf{L}^G \cdot \mathbf{R}^T. \quad (8)$$

The tensor  $\mathbf{\Omega}$  is equal to the spin tensor  $\mathbf{W}$  if the stretch tensor is symmetric. The second term of (8) is then equal to the symmetric rate of deformation tensor  $\mathbf{D}$ ,

$$\mathbf{L} = \mathbf{W} + \mathbf{D} = \frac{1}{2}(\mathbf{v} \bar{\nabla} - \bar{\nabla} \mathbf{v}) + \frac{1}{2}(\mathbf{v} \bar{\nabla} + \bar{\nabla} \mathbf{v}). \quad (9)$$

However, the decomposition of (4) does not necessarily result in a symmetric stretch tensor in which case  $\mathbf{\Omega}$  and  $\mathbf{W}$

will differ! This will be illustrated in Section 4. The rate of rotation tensor  $\dot{\mathbf{R}}$  is found by rewriting (5):

$$\dot{\mathbf{R}} = \mathbf{L} \cdot \mathbf{R} - \mathbf{R} \cdot \dot{\mathbf{G}} \cdot \mathbf{G}^{-1} = \boldsymbol{\Omega} \cdot \mathbf{R}. \quad (10)$$

## 2.2. Stresses and strains

The local stress tensor  $\boldsymbol{\tau}$  is introduced as

$$\boldsymbol{\tau} = \mathbf{e}_i \cdot \tau_{ij} \cdot \mathbf{e}_j, \quad (11)$$

with  $\mathbf{e}_i$  and  $\mathbf{e}_j$  the global base vectors. The local stress tensor  $\boldsymbol{\tau}$  co-rotates with the rigid body rotations of the axes of anisotropy, which result from the decomposition (4). The stress tensor  $\boldsymbol{\tau}$  is therefore invariant. It is related to the global Cauchy stress tensor  $\boldsymbol{\sigma}$  by a rotation only,

$$\boldsymbol{\sigma} = \mathbf{R} \cdot \boldsymbol{\tau} \cdot \mathbf{R}^T. \quad (12)$$

This approach was introduced by Huétink [13] and leads to a conceptually simple scheme for an updated or total Lagrange FE formulation for anisotropic materials. Nonlinearities due to reorientation of the material are taken into account when mapping the local stress tensor to the global Cauchy stress tensor. Constitutive laws can be written in terms of an invariant fourth order material tensor  ${}^4\mathbf{E}$ , where  ${}^4\mathbf{E}$  is constant in case of elastic deformations. There is no need for non-orthogonal constitutive equations as introduced by Yu [31] and Xue [30].

The right and left Cauchy Green tensor,  $\mathbf{C}$  and  $\mathbf{B}$  respectively, are suitable strain definitions for large deformations. Both strain measures equal unity in case of rigid body rotations. Using the decomposition of (4), the strain definitions can be written as

$$\mathbf{C} = \mathbf{F}^T \cdot \mathbf{F} = \mathbf{G}^T \cdot \mathbf{G}, \quad (13)$$

$$\mathbf{B} = \mathbf{F} \cdot \mathbf{F}^T = \mathbf{R} \cdot \mathbf{G} \cdot \mathbf{G}^T \cdot \mathbf{R}^T. \quad (14)$$

The rate of the right Cauchy Green tensor is related to the rate of deformation tensor  $\mathbf{D}$  according to

$$\dot{\mathbf{C}} = 2\mathbf{F}^T \cdot \mathbf{D} \cdot \mathbf{F} = 2\mathbf{G}^T \cdot \mathbf{R}^T \cdot \mathbf{D} \cdot \mathbf{R} \cdot \mathbf{G}. \quad (15)$$

The rate of the Cauchy stress (12) is related to the local stress and the local stress rate:

$$\dot{\boldsymbol{\sigma}} = \dot{\mathbf{R}} \cdot \boldsymbol{\tau} \cdot \mathbf{R}^T + \mathbf{R} \cdot \dot{\boldsymbol{\tau}} \cdot \mathbf{R}^T + \mathbf{R} \cdot \boldsymbol{\tau} \cdot \dot{\mathbf{R}}^T. \quad (16)$$

## 2.3. Plasticity

The total deformation is split into an elastic reversible part and a plastic irreversible part

$$\mathbf{F} = \mathbf{R} \cdot \mathbf{G}_e \cdot \mathbf{G}_p. \quad (17)$$

This results in a split of the velocity gradient  $\mathbf{L}^G$  (7) in an elastic part  $\mathbf{L}_e$  and plastic part  $\mathbf{L}_p$

$$\mathbf{L}^G = \mathbf{L}_e + \mathbf{L}_p, \quad (18)$$

with

$$\mathbf{L}_e = \dot{\mathbf{G}}_e \cdot \mathbf{G}_e^{-1}, \quad (19)$$

$$\mathbf{L}_p = (\mathbf{G}_e \cdot {}^4\mathbf{I} \cdot \mathbf{G}_e^{-T}) : \dot{\mathbf{G}}_p \cdot \mathbf{G}_p^{-1}, \quad (20)$$

where  ${}^4\mathbf{I}$  is a fourth order tensor having the property  ${}^4\mathbf{I} : \mathbf{A} = \mathbf{A}$ , where  $\mathbf{A}$  is an arbitrary second order tensor. Constitutive laws provide the additional equations to determine the quantitative split of the total deformation.

## 2.4. Free energy and stress

Constitutive equations can be successfully derived using the Helmholtz free energy, see e.g. Akkerman [1]. The starting point is some form of the Second Law of thermodynamics. There are no restrictions for the material response at large deformations, but the response at small deformations must coincide with the linear theory, see Huétink [12]. Huétink [13] showed that the free energy can be expressed as an invariant function of  $\mathbf{C}$  only in case of anisotropy, whereas that is not possible for the left Cauchy Green tensor  $\mathbf{B}$ . The free energy would then be a function of the tensor  $\mathbf{R}$  as well. This makes it more complicated to derive constitutive equations from free energy functions. Therefore  $\psi$  is regarded as a function of the elastic strain tensor  $\mathbf{C}_e$ .

$$\psi = \psi(\mathbf{C}_e). \quad (21)$$

The local stress tensor is derived from the free energy [13]:

$$\boldsymbol{\tau} = 2\rho\mathbf{G}_e \cdot \frac{\partial\psi}{\partial\mathbf{C}_e} \cdot \mathbf{G}_e^T. \quad (22)$$

## 3. Finite element formulation

The strong form of mechanical equilibrium without the presence of body forces and boundary traction is formulated as

$$\boldsymbol{\sigma} \cdot \vec{\nabla} = \mathbf{0}. \quad (23)$$

Following the standard procedure of weighing, applying reduced integration and the divergence theorem of Gauss, the weak form of (23) becomes:

$$\int_V \mathbf{w} \cdot \vec{\nabla} : \boldsymbol{\sigma} dV = \int_\Gamma \mathbf{w} \cdot \mathbf{t} d\Gamma, \quad (24)$$

where  $\mathbf{w}$  are the weight functions and  $\mathbf{t}$  is the traction on the boundary surface. The rate form of this equation in the current configuration is found to be

$$\int_V \left( \mathbf{w} \cdot \vec{\nabla} : \dot{\boldsymbol{\sigma}} - \mathbf{w} \cdot \vec{\nabla} \cdot \mathbf{v} \cdot \vec{\nabla} : \boldsymbol{\sigma} + \mathbf{w} \cdot \vec{\nabla} : \boldsymbol{\sigma} \frac{J}{J} \right) dV = \int_\Gamma \mathbf{w} \cdot \dot{\mathbf{t}} d\Gamma, \quad (25)$$

where  $J$  denotes the Jacobian, the volume ratio:

$$J = \det(\mathbf{F}) = \frac{dV}{dV_0}, \quad (26)$$

Eq. (25) is used to find consistent tangent matrices for the FE calculations.

#### 4. Fibre reinforced material

Section 2.1 stated the freedom of choice for the decomposition of the deformation tensor  $\mathbf{F}$  in a stretch tensor  $\mathbf{G}$  and a subsequent rotation  $\mathbf{R}$ . The mapping of the initial fibre  $\mathbf{a}_0$  onto its current state  $\mathbf{a}$  is given by

$$\mathbf{a} = \mathbf{F} \cdot \mathbf{a}_0 = \mathbf{R} \cdot \mathbf{G} \cdot \mathbf{a}_0. \quad (27)$$

In case of uniaxial fibres it is convenient to take a rotation  $\mathbf{R}$  that rotates the initial fibre direction  $\mathbf{a}_0$  towards the current fibre direction  $\mathbf{a}$ :

$$\mathbf{R} \cdot \mathbf{a}_0 = \frac{\ell_0}{\ell} \mathbf{a}. \quad (28)$$

The non-symmetrical tensor  $\mathbf{G}$  now relates the current length  $\ell$  to the initial length  $\ell_0$ :

$$\mathbf{G} \cdot \mathbf{a}_0 = \frac{\ell}{\ell_0} \mathbf{a}_0. \quad (29)$$

The fibres are assumed to be linearly elastic. The scalar fibre strain is defined as

$$\varepsilon = \frac{1}{2} \frac{\ell^2 - \ell_0^2}{\ell_0^2} \quad (30)$$

or using the right Cauchy Green tensor:

$$\varepsilon = \frac{1}{2} \mathbf{a}_0 \mathbf{a}_0 : (\mathbf{C}_e - \mathbf{1}) / \ell_0^2. \quad (31)$$

The resulting free energy function per unit mass equals the elastically stored energy.

$$\psi = \frac{1}{2\rho} E_f \varepsilon^2 = \frac{E_f}{8\rho_0 \ell_0^4} (\mathbf{C}_e - \mathbf{1}) : \mathbf{a}_0 \mathbf{a}_0 \mathbf{a}_0 \mathbf{a}_0 : (\mathbf{C}_e - \mathbf{1}). \quad (32)$$

Using (22), the invariant stress  $\tau$  is found to be

$$\tau = \frac{\rho E_f \ell^2}{2\rho_0 \ell_0^6} \mathbf{a}_0 \mathbf{a}_0 \mathbf{a}_0 \mathbf{a}_0 : (\mathbf{C}_e - \mathbf{1}) \quad (33)$$

and the Cauchy stress tensor:

$$\sigma = \frac{\rho E_f}{2\rho_0 \ell_0^4} \mathbf{a} \mathbf{a} \mathbf{a}_0 \mathbf{a}_0 : (\mathbf{C}_e - \mathbf{1}). \quad (34)$$

##### 4.1. Consistent tangent

The performance of implicit FE simulations depends largely on the consistency of the tangent (stiffness) matrix when using a Newton–Raphson procedure. The iterative process converges very slowly or even diverges if not all the nonlinearities are taken into account, especially when it concerns highly anisotropic materials.

The local stress rate is found by differentiating (33) with respect to time.

$$\dot{\tau} = \frac{\rho E_f \ell^2}{2\rho_0 \ell_0^6} \mathbf{a}_0 \mathbf{a}_0 \mathbf{a}_0 \mathbf{a}_0 : \dot{\mathbf{C}}_e + \tau \left( 2 \frac{\dot{\ell}}{\ell} + \frac{\dot{\rho}}{\rho} \right). \quad (35)$$

The rate of rotation tensor  $\dot{\mathbf{R}}$  results from combining (28), (29) and (10):

$$\dot{\mathbf{R}} = \mathbf{L} \cdot \mathbf{R} - \frac{\dot{\ell}}{\ell} \mathbf{R}. \quad (36)$$

Conservation of mass can be expressed as

$$\rho J = c. \quad (37)$$

This results in the following relation for the rates:

$$\frac{\dot{\rho}}{\rho} = -\frac{\dot{J}}{J}. \quad (38)$$

Eqs. (33), (35), (36) and (12) are now used to express the rate of the Cauchy stress (16). This rate is used in (25) and with (38) it results in the following consistent tangent matrix for the uniaxial fibre model:

$$K = \int_V \left[ \frac{\rho E_f}{\rho_0 \ell_0^6} \cdot \left( \frac{1}{2} (\mathbf{w} \overleftarrow{\nabla} + \overrightarrow{\nabla} \mathbf{w}) \cdot \mathbf{a} \mathbf{a} \right) : \left( \mathbf{a} \mathbf{a} \cdot \frac{1}{2} (\mathbf{v} \overleftarrow{\nabla} + \overrightarrow{\nabla} \mathbf{v}) \right) + \overrightarrow{\nabla} \mathbf{w} \cdot \mathbf{v} \overleftarrow{\nabla} : \sigma \right] dV. \quad (39)$$

#### 5. General elastic anisotropy

The free energy function  $\psi$  of the uniaxial fibre model (32) is extended to the arbitrary anisotropic case:

$$\psi = \frac{1}{8\rho_0} (\mathbf{C}_e - \mathbf{1}) : {}^4\mathbf{E} : (\mathbf{C}_e - \mathbf{1}), \quad (40)$$

with  ${}^4\mathbf{E}$  the invariant and constant fourth order material tensor. Using (22), the invariant stress  $\tau$  for the generalised anisotropic model is

$$\tau = \frac{\rho}{2\rho_0} (\mathbf{G}_e \cdot {}^4\mathbf{I} \cdot \mathbf{G}_e^T) : {}^4\mathbf{E} : (\mathbf{C}_e - \mathbf{1}). \quad (41)$$

##### 5.1. Consistent tangent

The rate of the local stress tensor (41) is given by

$$\dot{\tau} = \frac{\dot{\rho}}{\rho} \tau + {}^4\mathbf{E}^* : \mathbf{L}_e, \quad (42)$$

with

$${}^4\mathbf{E}^* = 4 \frac{\rho}{\rho_0} (\mathbf{G}_e \cdot {}^4\mathbf{I} \cdot \mathbf{G}_e) : {}^4\mathbf{E} : (\mathbf{G}_e^T \cdot {}^4\mathbf{I} \cdot \mathbf{G}_e^T) + {}^4\mathbf{I} \cdot \tau + \tau \cdot {}^4\mathbf{I}. \quad (43)$$

Since  ${}^4\mathbf{E}^*$  is symmetric, the skewsymmetric components of  $\mathbf{L}_e$  in (42) will vanish. The non-symmetric tensor  $\mathbf{L}_e$  can be replaced by its symmetric part, an invariant rate of deformation tensor  $\mathbf{d}_e$ :

$$\mathbf{d}_e = \frac{1}{2} (\mathbf{L}_e + \mathbf{L}_e^T) = \mathbf{R}^T \cdot \mathbf{D} \cdot \mathbf{R}. \quad (44)$$



The local stress rate can therefore be written as

$$\dot{\tau} = \frac{\dot{\rho}}{\rho} \tau + {}^4\mathbf{E}^* : \mathbf{d}_c. \quad (45)$$

Analogous to the procedure in Section 4.1, Eqs. (41), (45), (10) and (12) are now used to express the rate of the Cauchy stress (16). This rate is used in (25) and with (38) it results in the following consistent tangent matrix for the generalised anisotropic model:

$$K = \int_V \left[ \frac{\rho}{\rho_0} \cdot \frac{1}{2} (\mathbf{w} \bar{\nabla} + \bar{\nabla} \mathbf{w}) : (\mathbf{F} \cdot {}^4\mathbf{I} \cdot \mathbf{F}) : {}^4\mathbf{E} : (\mathbf{F}^T \cdot {}^4\mathbf{I} \cdot \mathbf{F}^T) : \frac{1}{2} (\mathbf{v} \bar{\nabla} + \bar{\nabla} \mathbf{v}) + \bar{\nabla} \mathbf{w} \cdot \mathbf{v} \bar{\nabla} : \boldsymbol{\sigma} \right] dV. \quad (46)$$

## 6. Application

The large deformation finite element formulation has been implemented in MATLAB<sup>®</sup> to examine the performance. Multiple convergence and accuracy tests were performed. The uniaxial tensile test example discussed in the introduction does not show unrealistic shapes anymore due to the correct update of the fibre direction. The fibre strain in the shear test example is now accurately predicted, independent of the number of steps or the size of the displacement increments. Two additional examples including plasticity will be discussed here: the bias extension experiment and the pressurisation of a McKibben actuator.

### 6.1. Bias extension

The bias extension experiment is frequently used to examine the shear response of biaxial reinforced materials. Fig. 5 shows the undeformed and the deformed shape of the material. The two fibre directions are initially perpendicular to each other at  $\pm 45^\circ$ . The specimen is gripped on the short edges and elongated in the  $0^\circ$  direction. The stiffness of the fibres is dominant and the specimen deforms as a trellis frame, with each fibre crossing acting as a possible hinge point. Three deformation regions develop: an undeformed region, a central region with pure shear and

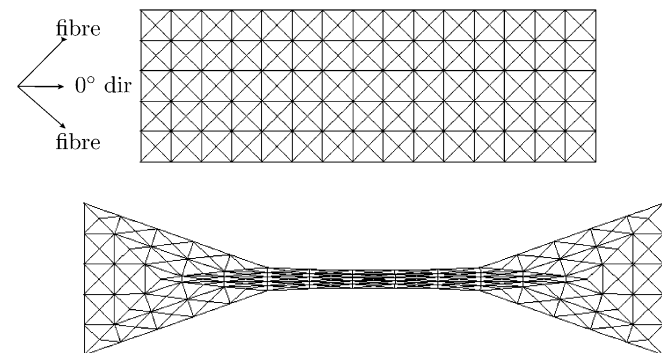


Fig. 5. The undeformed and deformed shape of the bias extension simulation (no displacement scaling).

a region with intermediate shear. Potter presented an extensive discussion of the bias extension experiment in [24].

The fabric is 70 mm wide, 210 mm long and has a thickness of 1 mm. It is meshed using 300 two-dimensional plane stress simplex triangles. Several material fractions are combined within one element in these simulations. The deformation is equal for each fraction and each fraction contributes to the total stress proportional to its volume fraction  $v$ :

$$\boldsymbol{\sigma} = \sum_i v_i \boldsymbol{\sigma}_i, \quad (47)$$

where  $i$  denotes the fraction number. The biaxial material is represented by an elastic isotropic bulk fraction and two fibre fractions, with a Young's modulus 1.0 GPa and  $1.0 \times 10^3$  GPa respectively. The deformation shown in Fig. 5 is applied in only one step, which is a good performance for an FE code. Fig. 6 shows the convergence behaviour of this simulation. The unbalance norm  $\epsilon_u$  and the displacement norm  $\epsilon_d$  are given by

$$\epsilon_u = \frac{\|R - F\|}{\|R\|}, \quad \epsilon_d = \frac{\|\Delta u\|}{\|u\|}, \quad (48)$$

where  $R$  are the reaction forces,  $F$  the applied nodal loads,  $\Delta u$  the displacement found during the iteration and  $u$  the total displacement. The simulation initially converges slowly, due to strain increments over 100% and fibre rotations up to  $45^\circ$ . After eight iterations it shows quadratic convergence. All individual steps converge to machine precision within six iterations if the simulation is split into more than three steps, showing quadratic convergence from the first iteration onwards.

Another large advantage of the nonlinear Cauchy Green strain definition is the increased robustness of the simulation when using poorly shaped elements. Fig. 5 shows elements with angles below  $2^\circ$ , but the simulation can be continued with another step without problems.

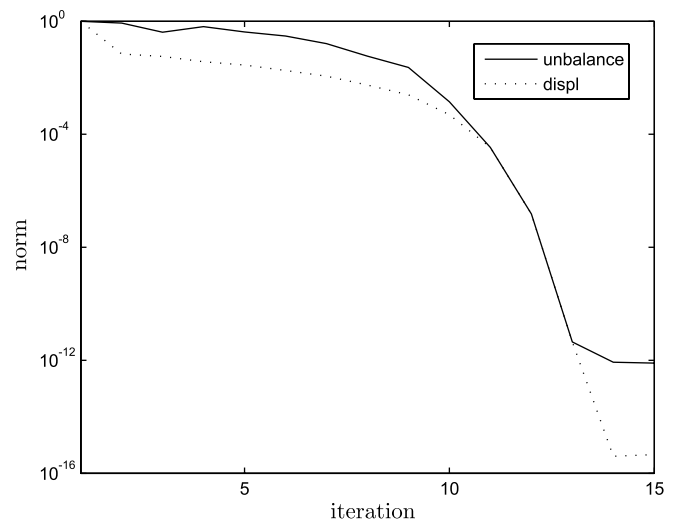


Fig. 6. Convergence plot of the one-step bias extension simulation from Fig. 5.

### 6.1.1. Plasticity and rigid rotations

Non-crimp fabrics (NCF) consist of separate fibre layers which are stitched together with a stitching thread. This thread is often made from polyester. An idealised model of the biaxial NCF is found in Fig. 7. The two fibre layers are orientated in the  $\pm 45^\circ$  direction and the stitching thread is orientated in the  $0^\circ$  direction. The stitch can deform plastically. A bias extension experiment as illustrated in Fig. 5 is no longer dominated by the shear response of the fabric, but by the response of the stitch thread. The thread is included in the simulation by an additional fibre fraction that can deform plastically according to the Nadai stress–strain curve shown in Fig. 8. The stitch responds elastically up to the yielding point and then follows the yield surface given by the yield stress  $\sigma_y$ :

$$\sigma_y = \sigma_0 + C(\varepsilon_0 + \varepsilon_p)^n, \quad (49)$$

where  $\sigma_0$ ,  $C$ ,  $\varepsilon_0$  and  $n$  are material parameters and  $\varepsilon_p$  denotes the plastic strain in the stitch material. The soft stitch material has been modelled using the following values: Young's modulus = 3.0 GPa,  $\sigma_0 = 30$  MPa,  $C = 100$  MPa,  $\varepsilon_0 = 5 \times 10^{-5}$  and  $n = 0.6$ .

The fabric is simultaneously rotated by  $90^\circ$  during the extension to illustrate the performance of the code under large rigid body rotations. Fig. 9 shows the deformed shape of the specimen. The colours indicate the plastic strain in the stitches, going up to 40%. The total deformation and rotation is applied in two steps and the individual steps converged to machine precision within eight iterations. This illustrates that the formulation works very well for large deformations and rotations including plasticity as well.

### 6.2. McKibben actuator

The McKibben actuator is a pneumatic actuator with a high power to weight ratio and used as an artificial muscle or as an actuator in mobile robots. It consists of a inner bladder made of a flexible material, covered by a braided shell with two fibre families. These fibre families have an equal but opposite angle with respect to the longitudinal axis. The actuator expands radially if it is pressurised and contracts or expands longitudinally, depending on the initial orientation of the fibres. The angle of the fibres with respect to the longitudinal axis will approach the theoretic

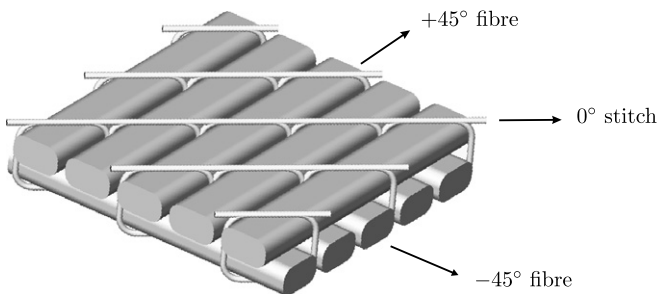


Fig. 7. Idealised model of a biaxial non-crimp fabric: two fibre layers and a stitching thread.

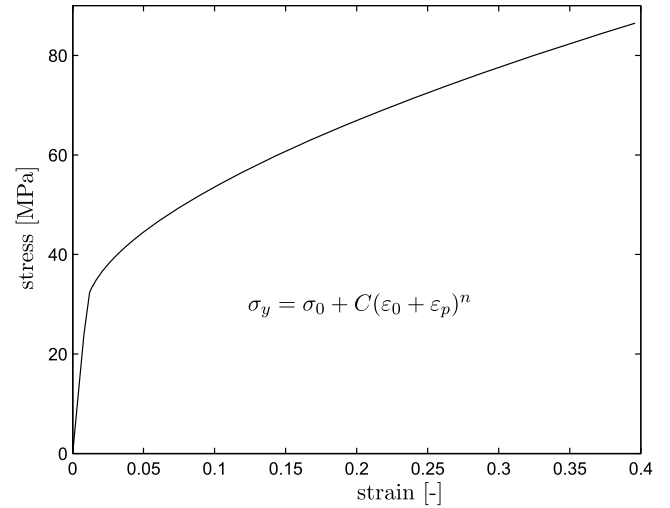


Fig. 8. Stress–strain curve of a polyester stitching thread with Nadai hardening. Young's modulus = 3.0 GPa,  $\sigma_0 = 30$  MPa,  $C = 100$  MPa,  $\varepsilon_0 = 5 \times 10^{-5}$ ,  $n = 0.6$ .

cal limit of  $54.4^\circ$  at infinite pressure, based on the stress distribution in longitudinal and circumferential direction of a thin pressurised vessel covered with inextensible fibres. This implies that actuators with initial fibre angles below  $54.4^\circ$  will contract during pressurisation, respectively expand for angles above  $54.4^\circ$ .

Experimental and mathematical analyses of actuators made from natural latex rubber bladders and polyester braids were conducted by Klute in 2000 [14]. One of his experiments has been simulated in a three-dimensional simulation. Fig. 10 shows the actuator at ambient pressure and at a pressure of 21.5 bars. The initial length, radius and thickness of the actuator are respectively 264.0 mm, 8.7 mm and 2.4 mm. The end caps are considered to be rigid. The initial fibre angle with respect to the longitudinal axis is  $17.69^\circ$ . The actuator is meshed with 2480 plane stress triangular membrane elements and loaded with a uniform pressure from the inside. The bladder material is modelled using a Mooney–Rivlin material model in which the stored strain energy  $W$  can be expressed as

$$W = \sum_{i=0, j=0}^n C_{ij} (I_1 - 3)^i (I_2 - 3)^j, \quad (50)$$

where  $C_{ij}$  are empirical constants and  $I_1$  and  $I_2$  are the strain invariants of the left Cauchy strain tensor  $\mathbf{B}$ . Two constants are sufficient to model the bladder material accurately and are given by Klute:  $C_{10} = 118.4$  kPa and  $C_{01} = 105.7$  kPa. Klute considered the fibres to be inextensible, a condition that is imposed by setting the Young's modulus of the fibres to 100 GPa. This result in a stiffness ratio between the two material fractions of approximately  $10^6$ , causing the system to be ill conditioned with condition numbers around  $10^7$ . In spite of the large condition numbers, the simulation runs without adding inertia effects. Inertia effects have a positive effect on the stability and speed of the simulation as mentioned in the research of Meinders et al. [18].

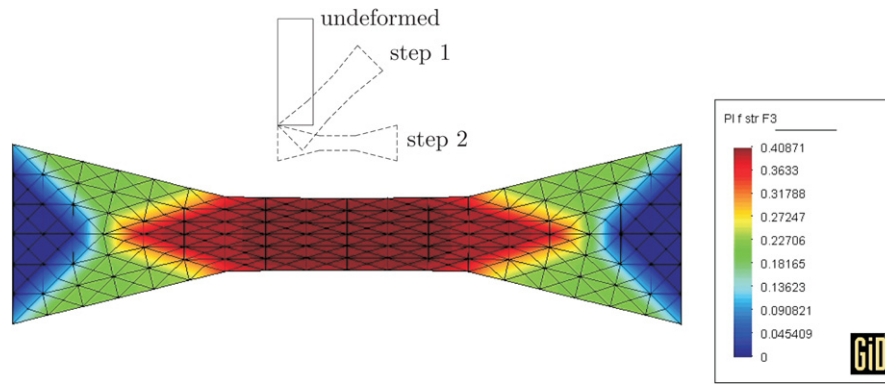


Fig. 9. Plastic strain in the polyester stitching thread during a bias extension and simultaneous rotation of a non-crimp fabric.

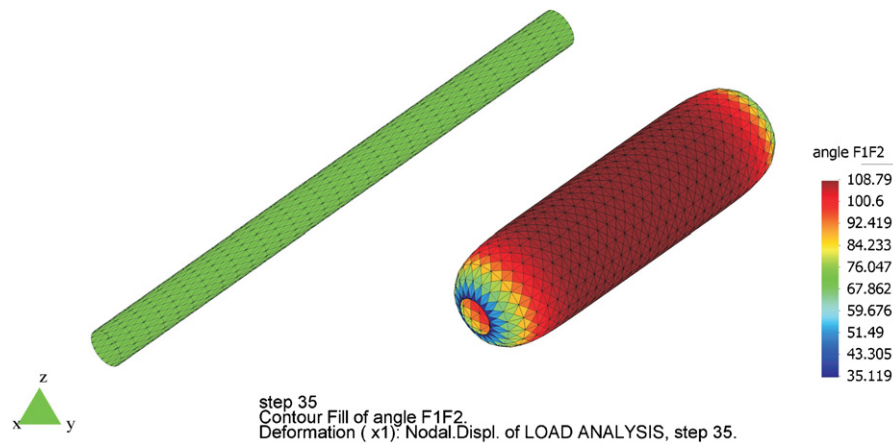


Fig. 10. A McKibben actuator at ambient pressure and at 21.5 bars.

The actuator is pressurised up to 100 bars in 40 steps. Fig. 10 shows the pressurised actuator at its minimal length at a pressure of 21.5 bars. The plot shows the angle between the two fibre families, which is twice the angle with respect to the longitudinal axis. The angle approaches the theoretical limit discussed before. The actuator expands radially and longitudinally if the pressure is increased above 21.5 bars, while the angle remains constant. Analytical expressions for actuator forces at different contraction ratios were given by Gaylord in 1958 [7]. Gaylord assumed inextensible fibres and neglected the membrane deformations of the inflated bladder. The model results in a theoretical upper bound. Klute developed a nonlinear model that incorporates the membrane deformations of a Mooney–Rivlin bladder material as well. The results from both analytical models and the FE results are plotted in Fig. 11 for this specific actuator at a pressure of 5 bars. The contraction ratio  $\lambda$  is defined as the ratio between the current length and the length at ambient pressure:  $\lambda = L/L_0$ . The FE model shows good agreement with the model developed by Klute, although deviations with the experimental results are still significant. This can be due to elastic and/or plastic strain in the fibres. The braid manufacturer (Alpha Wire Company) kindly supplied further details on the reinforcement used. The GRP-110-1-1/4 braid consists of thermo-

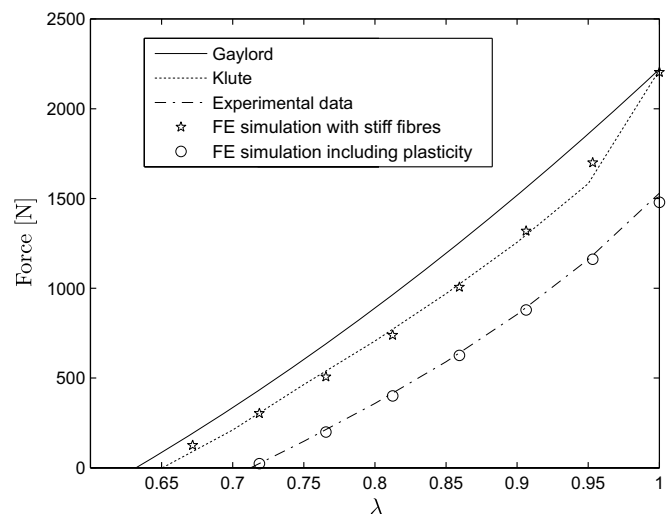


Fig. 11. Actuator force at a pressure of 5 bars.

plastic polyester fibres and has a linear density of 24 g/m. The polyester has a density of 1340 kg/m<sup>3</sup>. These values result in fibre stresses between 140 and 150 MPa, well above the elastic region of polyester. The simulation has been rerun including fibre plasticity and a hardening law according to Nadai: Young's modulus = 3.5 GPa,  $\sigma_0 =$



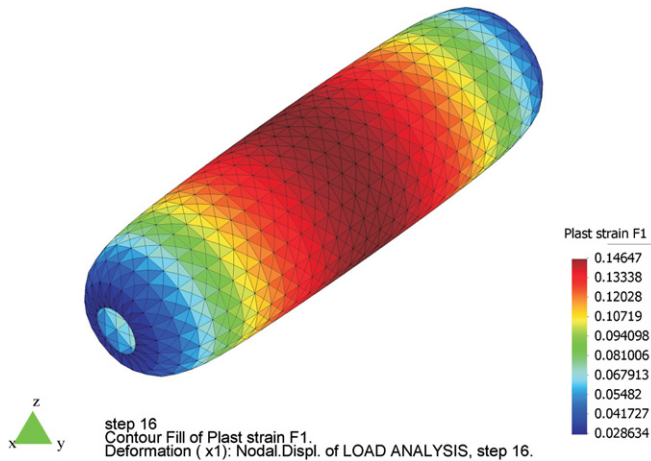


Fig. 12. Total plastic fibre strain at a pressure of 5 bars.

70 MPa,  $C = 350$  MPa,  $\varepsilon_0 = 5 \times 10^{-5}$  and  $n = 0.6$ . The fibres start yielding when the pressure exceeds 2.5 bar. Fig. 12 shows the plastic fibre strain distribution along the actuator at a pressure of 5 bars. The permanent plastic strain in the fibre reduces the actuator force and the force now corresponds to the experimental results as shown in Fig. 11. Accurate stress strain curves for this material should be obtained to validate the hypotheses of fibre yielding at these pressure levels. This example illustrates that the method works properly for 3D membrane elements with in and out of plane loading including plastically deformable fibres. The simulations are robust and show quadratic convergence, provided the pressure boundary condition is linearised consistently.

## 7. Numerical issues

Fig. 6 shows a displacement norm that reduces to machine precision. The unbalance norm remains  $10^3$  times higher. This is due to the condition of the system. The fibre stiffness is  $10^3$  times higher than the bulk stiffness, causing unbalances in the same order of magnitude.

Care should also be taken when storing the deformation gradient  $\mathbf{F}$ . Large rounding errors can occur if deformations are small and the deformation gradient and the right Cauchy Green strain tensor are close to unity. Significant digits are lost when the local stress  $\boldsymbol{\tau}$  is evaluated (41), due to the subtraction of the unit tensor  $\mathbf{I}$ . This can be solved by writing:

$$\mathbf{F} = \mathbf{I} + \delta\mathbf{F}. \quad (51)$$

Storing  $\delta\mathbf{F}$  instead of  $\mathbf{F}$  and rewriting the strain definition in terms of  $\delta\mathbf{F}$  avoids the large numerical rounding errors if small deformations are applied.

A shell or membrane formulation is commonly used in forming simulations of thin sheet materials, the so called 2.5-dimensional case. Strain in the out of plane direction is evaluated using constitutive equations and assuming plane stress conditions. Eqs. (39) and (46) show that the

tangent stiffness matrices are generally symmetric, but in the 2.5-dimensional case this is only true if the volume or the thickness is assumed to be constant. Other assumptions will result in a non-symmetrical tangent matrix.

## 8. Conclusions

The standard finite element codes are not very suitable for large deformation simulations of highly anisotropic materials. It leads to confusing formulations as well. To avoid misalignment of the nodal forces, the material axes of anisotropy should be evaluated on the final geometry. However, this causes the accuracy of the strain prediction to drop significantly. Instead, the deformation gradient should be decomposed into a rotation tensor and a stretch tensor. The rotation reflects the rotation of the axes of anisotropy. This is an advantage when modelling fibre reinforced composites. Stresses are computed using invariant local stress and stiffness tensors. This leads to a simple and straightforward implementation of constitutive laws, which do not have to account for any rotation of the material. Consistent tangent matrices were presented for linearly elastic fibres and for a generalised anisotropic material. The scheme was implemented and tested in 2D and 3D simulations, including plasticity and large rigid rotations. The simulations converge quadratically for arbitrary deformation gradients and arbitrary degrees of anisotropy. The simulations are more robust than the standard implementations. Poorly shaped elements behave significantly better when using the right Cauchy Green strain definition instead of a linear strain definition.

## References

- [1] R. Akkerman, Euler–Lagrange Simulations of Nonisothermal Viscoelastic Flows. Ph.D. Thesis, University of Twente, The Netherlands, 1993. ISBN 90-9006764-7.
- [2] M. Aono, D.E. Breen, M.J. Wozny, Modeling methods for the design of 3d broadcloth composite parts, *Comput.-Aided Des.* 33 (2001) 989–1007.
- [3] F. Barlat, D.J. Lege, J.C. Brem, A six component yield function for anisotropic materials, *Int. J. Plast.* 7 (1991) 693–712.
- [4] Philippe Boisse, Meso-macro approach for composites forming simulation, *J. Mater. Sci.* 41 (2006) 6591–6598.
- [5] J. Bonet, A.J. Burton, A simple orthotropic, transversely isotropic hyperelastic constitutive equation for large strain computations, *Comput. Methods Appl. Mech. Engrg.* 162 (1998) 151–164.
- [6] B. Chen, M. Govindaraj, A physically based model of fabric drape using flexible shell theory, *Textile Res. J.* 65 (1995) 324–330.
- [7] R.H. Gaylord, Fluid actuated motor system and stroking device, US Patent 2,844,126, July 22 1958.
- [8] S.G. Hancock, K.D. Potter, The use of kinematic drape modelling to inform the hand lay-up of complex composite components using woven reinforcements, *Comp. Part A: Appl. Sci. Manufact.* 37 (2006) 413–422.
- [9] S.G. Hancock, K.D. Potter, Virtual fabric placement – a new strategy for simultaneous preform design, process visualisation and production of manufacturing instructions for woven composite components, in: *Proceedings on the 9th International ESAFORM Conference on Material Forming*, Publishing House Akapit, Krakow, Poland, 2006, ISBN 83-89541-66-1, pp. 727–730.

- [10] R. Hill, A theory of the yielding and plastic flow of anisotropic metals, *Proc. Roy. Soc. London* 193 (1948) 281–297.
- [11] Shih-Wei Hsiao, Noboru Kikuchi, Numerical analysis and optimal design of composite thermoforming process, *Comput. Methods Appl. Mech. Engrg.* 177 (1999) 1–34.
- [12] J. Huétink, On the simulation of thermo-mechanical forming processes, Ph.D. Thesis, University of Twente, the Netherlands, 1986.
- [13] J. Huétink, On anisotropy, objectivity and invariance in finite thermo-mechanical deformations, in: *Proceedings on the 9th International ESAFORM Conference on Material Forming*, Publishing House Akapit, Krakow, Poland, 2006, ISBN 83-89541-66-1, pp. 355–358.
- [14] G.K. Klute, B. Hannaford, Accounting for elastic energy storage in McKibben artificial muscle actuators, *ASME J. Dyn. Syst. Measure. Control* 122 (2000) 386–388.
- [15] Jia Lu, Panayiotis Papadopoulos, A covariant formulation of anisotropic finite plasticity: theoretical developments, *Comput. Methods Appl. Mech. Engrg.* 193 (2004) 5339–5358.
- [16] C. Mack, H. Taylor, The fitting of woven cloth to surfaces, *J. Textile Inst.* 47 (1956) 477–487.
- [17] S.P. McEntee, C.M. Brdaigh, Large deformation finite element modelling of single-curvature composite sheet forming with tool contact, *Comp. Part A: Appl. Sci. Manufact.* 29 (1998) 207–213.
- [18] T. Meinders, A.H. van den Boogaard, J. Huétink, Improvement of implicit finite element code performance in deep drawing simulations by dynamics contributions, *J. Mater. Process. Technol.* 134 (2003) 413–420.
- [19] B. Nedjar, Frameworks for finite strain viscoelastic-plasticity based on multiplicative decompositions. Part I: Continuum formulations, *Comput. Methods Appl. Mech. Engrg.* 191 (2002) 1541–1562.
- [20] B. Nedjar, Frameworks for finite strain viscoelastic-plasticity based on multiplicative decompositions. Part II: Computational aspects, *Comput. Methods Appl. Mech. Engrg.* 191 (2002) 1563–1593.
- [21] B. Nedjar, An anisotropic viscoelastic fibrematrix model at finite strains: Continuum formulation and computational aspects, *Comput. Methods Appl. Mech. Engrg.* 196 (2007) 1745–1756.
- [22] X.Q. Peng, J. Cao, A continuum mechanics-based non-orthogonal constitutive model for woven composite fabrics, *Comp. Part A: Appl. Sci. Manufact.* 36 (2005) 859–874.
- [23] P. Potluri, S. Sharma, R. Ramgulum, Comprehensive drape modelling for moulding 3d textile preforms, *Comp. Part A: Appl. Sci. Manufact.* 32 (2001) 1415–1424.
- [24] Kevin Potter, Bias extension measurements on cross-plyed unidirectional prepreg, *Comp. Part A: Appl. Sci. Manufact.* 33 (2002) 63–73.
- [25] S. Reese, Meso-macro modelling of fibre-reinforced rubber-like composites exhibiting large elastoplastic deformation, *Int. J. Solids Struct.* 40 (2003) 951–980.
- [26] Carlo Sansour, Jozef Bocko, On the numerical implications of multiplicative inelasticity with an anisotropic elastic constitutive law, *Int. J. Numer. Methods Engrg.* 58 (2003) 2131–2160.
- [27] S.B. Sharma, M.P.F. Sutcliffe, A simplified finite element model for draping of woven material, *Comp. Part A: Appl. Sci. Manufact.* 35 (2004) 637–643.
- [28] A. Spencer, Theory of fabric-reinforced viscous fluids, *Comp. Part A: Appl. Sci. Manufact.* 31 (2000) 1311–1321.
- [29] H. Vegter, A.H. van den Boogaard, A plane stress yield function for anisotropic sheet material by interpolation of biaxial stress states, *Int. J. Plast.* 22 (2006) 557–580.
- [30] Pu Xue, Xiongqi Peng, Jian Cao, Non-orthogonal constitutive model for characterizing woven composites, *Comp. Part A: Appl. Sci. Manufact.* 34 (2003) 183–193.
- [31] Woong-Ryeol Yu, Philip Harrison, Andrew Long, Finite element forming simulation for non-crimp fabrics using a non-orthogonal constitutive equation, *Comp. Part A: Appl. Sci. Manufact.* 36 (2005) 1079–1093.